Effect of nitrogen atmosphere on the printability, microstructure, precipitation, and mechanical properties of laser powder bed fused Fe-*x*Cr alloys

Siyuan Wei[1,*], Delvin Wuu[1], Verner Soh[1], Kwang Boon Lau[1], Fengxia Wei[1], Konstantinos A. Liogas[1,2], Baicheng Zhang[3], Qiang Zhu[1], Chee Koon Ng[1], Alexander M. Korsunsky[2], Pei Wang[1,4,*], Upadrasta Ramamurty[1,5]

[1] *Institute of Materials Research and Engineering (IMRE), Agency for Science, Technology and Research (A*STAR) , 2 Fusionopolis Way, Innovis #08-03, Singapore 138634, Republic of Singapore.*
[2] *MBLEM, Department of Engineering Science, University of Oxford, Parks Road, Oxford OX1 3PJ, United Kingdom*
[3]*Advanced Material & Technology Institute, University of Science and Technology Beijing, Beijing 100083, P.R. China.*
[4]*Engineering Cluster, Singapore Institute of Technology, Singapore 519961, Republic of Singapore.*
[5] *School of Mechanical and Aerospace Engineering, Nanyang Technological University, Singapore 639798, Republic of Singapore.*

* Co-corresponding authors: wei_siyuan@imre.a-star.edu.sg, wangp@imre.a-star.edu.sg

Abstract: The role of the nitrogen atmosphere on the microstructure and tensile properties of laser powder bed fused (PBF-LB/M) Fe-*x*Cr (*x*=0, 5, 10, 15, 24 wt.%, mixed using elemental Fe and pre-alloyed Fe-46 wt.% Cr powders) binary alloys was investigated and compared with those fabricated under an inert (argon) atmosphere. Microstructural characterization reveals the variations of grain morphology with the chemical composition and the distinct effects of nitrogen on grain refinement and texture. Additionally, PBF-LB/M performed under the nitrogen atmosphere leads to the formation of Cr and Fe nitrides in the alloy. Significant enhancements in strength were observed in Fe, Fe-5Cr, and Fe-10Cr fabricated under nitrogen atmosphere due possibly to the solid solution and precipitation strengthening caused by dissolved nitrogen and the nitrides, respectively. However, the Fe-15Cr and Fe-24Cr alloys processed under the nitrogen atmosphere are brittle and crack upon PBF-LB/M due to the residual stresses. The findings in this work enrich the understanding of the effects of fabrication atmospheres in additive manufacturing, insights of which can be extended to diverse categories of alloys.

Keywords: laser powder bed fusion; solidification microstructure; synchrotron radiation; nitrides; mechanical properties.

1. Introduction

The advantages brought forth by additive manufacturing (AM) of metals, using techniques such as laser powder bed fusion (PBF-LB/M), from the manufacturing perspectives are now widely known. From the metallurgical perspective, due to the 'bottom-up' nature of manufacturing near-net shaped components, it offers additional degrees of freedom for meso- and microstructural design by varying the process parameters such as the laser power, scan speed, and scan rotation [1-3]. One can also vary the physical conditions such as heating the substrate [4,5], imposing a magnetic field [6], or subjecting the PBF-LB/M process to ultrasonic treatment [7], for the above purpose. In this context, varying the protective atmosphere has also been explored [8-11]. Its implementation is straightforward as no complex alternation on the printing machine is required. However, its utility, especially in Fe-based alloys, remains largely unexplored.

Nitrogen is known for enhancing the mechanical properties of steels. As interstitial solute atoms, nitrogen hardens the materials via solid solution strengthening [12,13]. Interestingly, it enhances the fracture toughness, possibly by increasing the electron state density at the Fermi level, which promotes nondirectional metallic bonding [13,14]. Through surface treatment, nitrogen can also be incorporated to the alloys as nitrides, which harden the surface significantly [15,16]. Several different approaches can be utilized in PBF-LB/M for introducing nitrogen into steels, e.g., addition of nitride particles to the powder mixture [17], conducting gas atomization of powders under a nitrogen atmosphere [18,19], and utilizing nitrogen as protective atmosphere during printing [13,18]. While recent studies reveal the effect of nitrogen on commercial steels processed using PBF-LB/M, the complex chemical compositions of such steels (typically more than 5 alloying elements) make it challenging to fully understand the interaction between nitrogen and the other alloying elements. Some key issues remain unexplored. For example, would the high cooling rate and high energy input of the PBF-LB/M affect the solubility and existence form of the nitrogen (solute atoms or nitrides)? What is the role that alloying element plays, when interacting with nitrogen during PBF-LB/M?

Keeping this in view, binary Fe-Cr alloys were selected as the target materials, and printing under nitrogen atmosphere was chosen as the approach to introduce nitrogen during PBF-LB/M process. The rationales behind the research strategy are as follows. (i) Cr is known to increase the concentration of nitrogen and therefore commonly used in nitrogen steels [20,21], due to the strong Cr-N interaction [21,22]. (ii) Compared to other methods, utilizing nitrogen as the atmosphere during PBF-LB/M is more straightforward and can be conveniently

applied to varying materials systems. (iii) Studying the binary Fe-Cr alloys instead of steels with complex compositions can help in firmly establishing the cause-effect relations. Here, the Fe-*x*Cr (*x* up to 24 wt.%) alloys fabricated under the nitrogen atmosphere were studied and compared with those processed under an argon atmosphere, in order to reveal the effect of nitrogen on the key aspects of the PBF-LB/M alloys, e.g., printability, microstructure, precipitation, and mechanical properties. Significant effects of nitrogen atmosphere were uncovered after comprehensive characterizations. The revealed interactions between the nitrogen atmosphere and the Fe-Cr alloys are in distinct contrast to those in the conventional manufactured alloys, indicating the unique effects of the PBF-LB/M process.

2. Experiment

A Trumpf TruPrint 1000 PBF-LB/M machine was utilized for fabricating the Fe-*x*Cr alloys (*x*=0, 5, 10, 15, 24 wt.%), using elemental Fe (average diameter ~22.8 μm) and pre-alloyed Fe-46 wt.% Cr powders (average diameter ~32.5 μm) as feedstock. Both the feedstock powders were prepared using gas atomization under Ar atmosphere and have spherical shapes. The powders are physically mixed in a roller mill for 12 h to achieve homogeneous distribution. One example of Fe-10 wt.% Cr powder mixture (characterized using scanning electron microscopy (SEM)) is given in Figure 1. Blocks with size 10×20×30 mm^3 of each predetermined composition were fabricated under either Ar or N_2 atmospheres, with gas flow rate of 2 m/s. The samples will be referred to by their composition and printing atmosphere hereafter. For example, Fe-5Cr(N) refers to the alloy with the Fe-5 wt.% Cr fabricated under N_2 atmosphere. For process parameter optimization, laser power (120, 150, and 175 W), hatch spacing (70 and 100 μm), and scan speed (200, 240, and 300 mm/s) were varied. The following fabrication parameter combination, which resulted in the minimum porosity (≤ 1%) and no delamination or cracking, were selected for all the samples: laser spot diameter d=30 μm, laser wavelength λ=1064 nm, laser power w=175 W, layer thickness t=30 μm, hatch spacing l=70 μm, laser scan speed v=300 mm/s, and scan rotation θ=67°.

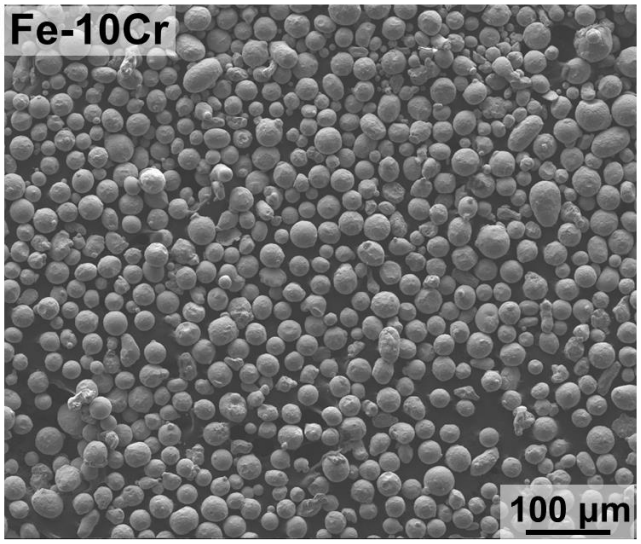

Figure 1. Representative secondary electron images of Fe-10 wt.% Cr powder mixture, showing homogeneous powder distribution.

Metallographic inspection (using optical microscopy) was conducted on the mechanically mirror-polished samples to measure the porosity levels in them. At least five images were taken for each condition. A SEM equipped with back-scattered electron (BSE), energy-dispersive X-ray spectroscopy (EDS), and electron backscatter diffraction (EBSD) detectors were utilized for microstructural characterizations, which were operated at the accelerating voltages of 15, 20, and 20 kV, respectively. A small step size of 0.5 μm was utilized for EBSD mapping to reveal the grain structures. Transmission electron microscopy (TEM) was further utilized to investigate the precipitates. The TEM specimens with thickness of ~50 nm were prepared using Ar-ion milling and the following combinations of ion energy (keV) and beam angle: 6 & 5°, 4 & 4°, and 2 & 2°.

Tensile testing was conducted on flat dog-bone samples (gauge dimensions: 6×1×2 mm^3) at a nominal strain rate of 10^{-3} s^{-1}. At least three tests were conducted for each condition. Note that the gauge dimensions of the tensile specimens do not conform to either the ASTM or ISO standards that are designed for bulk, conventionally manufactured alloys, as the geometrically complex shapes of the AM components, featured by heterogeneous microstructures and non-uniform section thicknesses make it challenging to strictly follow. To address this issue, non-standard miniature tensile testing specimens have been increasingly adopted and ASTM is developing new tensile testing standard for AM alloys (ASTM WK75901).

Synchrotron diffraction experiments (Figure 2(a)) were conducted on cylindrical Fe-Cr samples (10 mm diameter and 1 mm thickness) using the I12-JEEP beam line (wavelength of 0.0099975 nm), Diamond Light Source. Monochromatic beam energy was set to 124 keV with a spot size of 500 × 500 μm^2. The cylindrical samples were mounted statically on a plate (see Figure 2(b)), forming an array of 10 samples vertical to the incident beam, such that travels through the build direction (see Figure 2(c)) of them. By moving along the X and Y axes, large area diffraction mapping was conducted covering the central volume of the samples. Debye-Scherrer ring patterns were recorded using a large 2D area diffraction detector Pilatus 2M CdTe sitting behind the sample. The integration range for every sample was 40° to 160°, to ensure that the software integration limits were visible for every Debye-Scherrer ring 2D image in the GSAS II graphical user interface.

The nitrogen and oxygen contents of the samples were measured using the inert gas fusion technique in a LECO ONH Determinator. More specifically, the samples (after removing oxides layer and surface cleaning) were fused at 3000 °C in a high-purity graphite crucible under the protection of purified helium gas. Subsequently, the liberated analyte gas was swept out of the furnace by the helium gas to a series of detectors, where nitrogen and oxygen contents were measured by thermal conductivity detector and non-dispersive infrared cells, respectively.

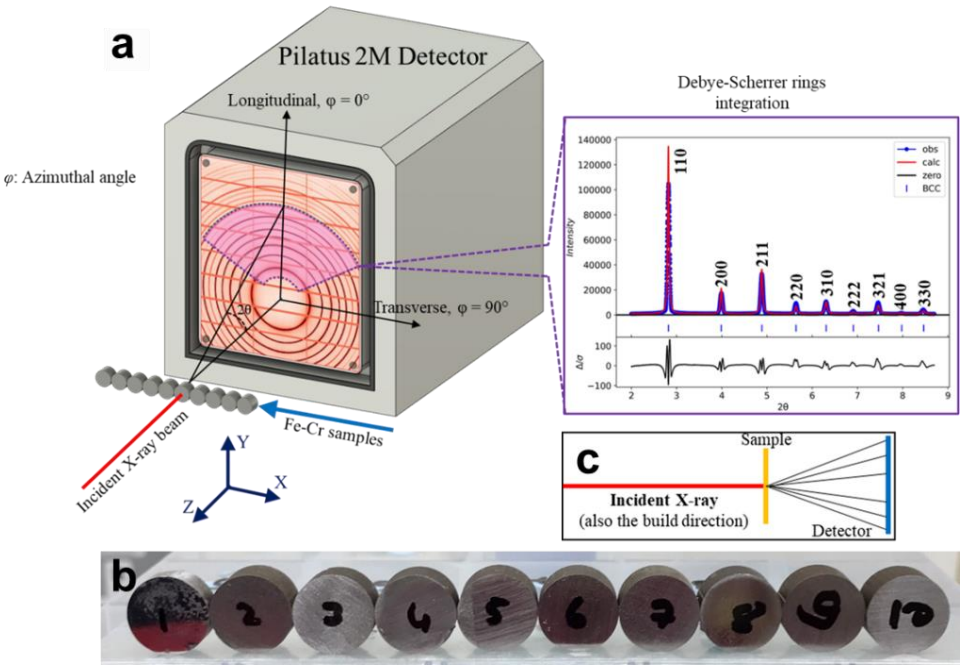

Figure 2. (a) The single shot synchrotron X-ray diffraction measurements. All 2D patterns from the mapping area were merged to a single 1D pattern, and the Rietveld analysis was performed using the GSAS-II software [23]. (b) Pictures of the Fe-*x*Cr sample for single-shot synchrotron. (b) Synchrotron measurement schematic.

3. Results and discussion

3.1.Nitrogen uptake and precipitation

Five different compositions, based on the Fe-Cr binary phase diagram (Figure 3(a)), were selected with the following rationale. (i) Fe, Fe-5Cr, and Fe-10Cr undergo a face centered cubic (FCC; γ) to a body centered cubic (BCC; α) solid-state phase transformation after solidification. While Fe-5Cr highlights the effect of Cr on such a transformation, Fe-10Cr experiences γ→α+γ→α transformation during cooling. (ii) Both Fe-15Cr and Fe-24Cr solidify without experiencing any γ→α phase transformation. However, in Fe-24Cr, dual phase microstructure with α+σ (close packed tetragonal; an intermetallic compound) phases is expected. (iii) As shown by the phase diagram, 24 wt.% Cr is close to the upper limit of composition range where the melting temperature remains constant and no noticeable distinction can be seen between the solidus and liquidus. This indicates the solidification processes of the examined compositions are likely to be similar and the effect of constitutional supercooling is insignificant.

The Cr contents in the Fe-*x*Cr alloys, obtained using EDS, are listed in Table 1. The compositions of the printed alloys correspond well with the expected ones. However, in situ alloying (using mixed powders) inevitably introduces chemical heterogeneity into the fabricated parts, due to one or more of the following reasons: un-melted particles [24], varying minor powders within melt pools [25], and insufficient physical/chemical mixing [26,27]. It is worth noting that Cr has a higher melting point (1907 °C) than Fe (1538 °C), which could lead to un-melted Cr particles, when elemental Cr and Fe powders are used. To circumvent such a possibility, pre-alloyed Fe-46 wt.%Cr powder was used as the source for Cr, which, according to the Fe-Cr binary phase diagram, has a similar melting point to Fe. Another advantage of using the pre-alloyed Fe-Cr power is that the level of Cr segregation can be alleviated, when compared to the use of elemental Cr powder. Detailed discussion on the chemical heterogeneity and its effect is given in section 3.2.1.

Although solidification during PBF-LB/M occurs under non-equilibrium conditions due to high thermal gradient and rapid cooling, the equilibrium phase diagrams can provide valuable insights on the solid-state phase transformations that may take place and constitutional undercooling [28,29]. To examine whether the phase variations in each PBF-LB/M alloy occur according to that expected from the equilibrium phase diagram, the printed samples were examined using synchrotron diffraction, and the results are shown in Figure 3(b). It is noted that only α phase exists in all the samples, despite the variations in composition and printing

atmosphere. Neither γ nor σ phases was detected. While the absence of the former is in accordance with the phase diagram, it is possible that the rapid solidification conditions that prevail during PBF-LB/M prevent the precipitation of σ in Fe-24Cr.

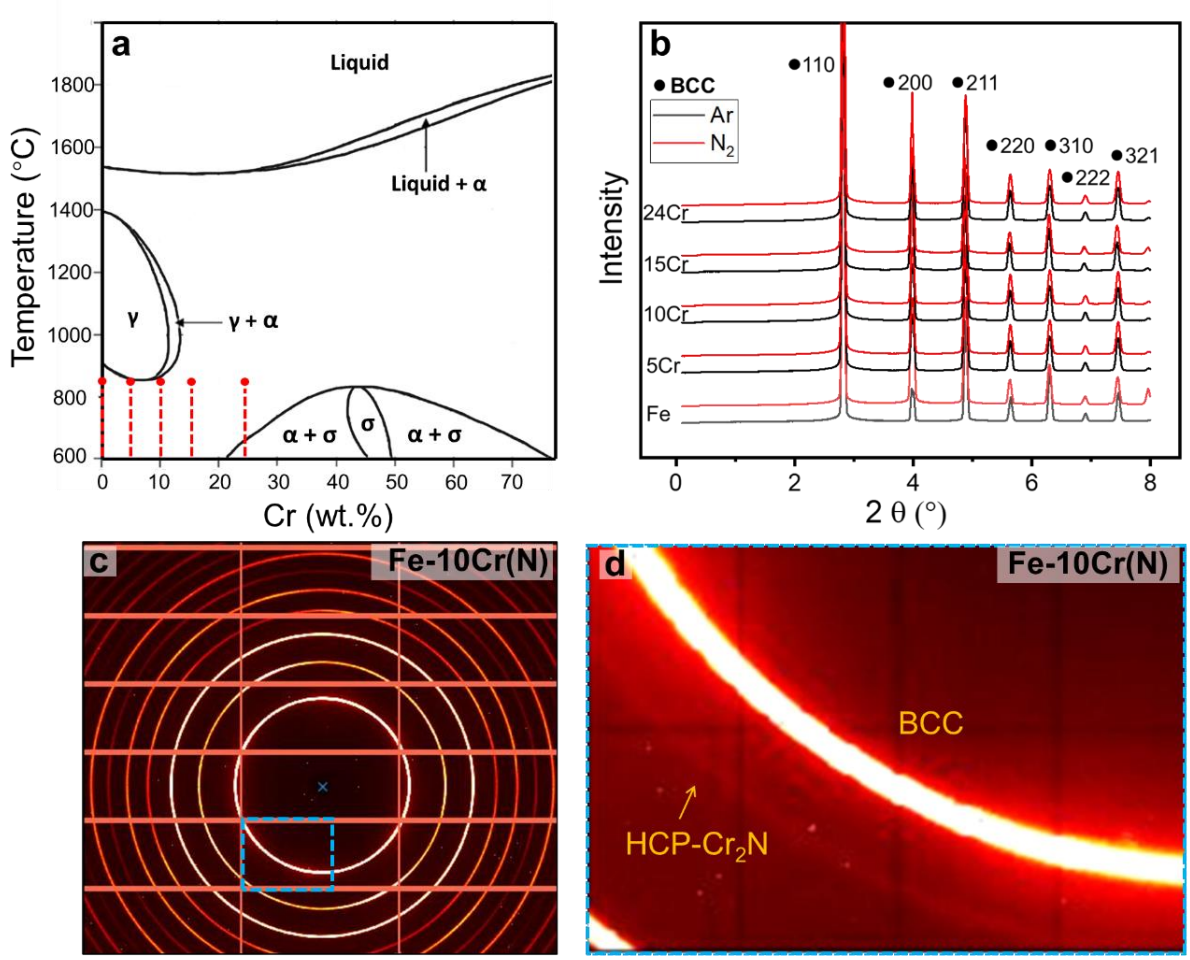

Figure 3. (a) Fe-Cr phase diagram (adopted from [30]). Compositions that are examined in this work are highlighted in red. (b) Synchrotron diffraction patterns of Fe-*x*Cr alloys (*x*=0, 5, 10, 15, 24 wt.%), fabricated under both argon and nitrogen atmosphere. (c) Debye-Scherrer ring patterns of Fe-10Cr(N). (d) Zoomed-in image of the area highlighted by blue dashed lines in (c), showing the vague ring of Cr_2N precipitates with hexagonal close packed (HCP) structure.

Table 1. Cr and N contents, relative densities, and grain sizes of Fe-*x*Cr alloys (*x*=0, 5, 10, 15, 24 wt.%).

Alloy		Cr content (wt.%)	Relative density (%)	N (wt.%)	Grain size (μm)
Fe	Ar	/	99.4 ±0.2	0.011±0.002	4.2±0.5
	N_2	/	99.5 ±0.1	0.053±0.002	3.9±0.7
Fe-5Cr	Ar	4.8 ±0.9	99.2 ±0.3	0.013±0.003	2.1±0.4
	N_2	5.0 ±0.8	99.3 ±0.2	0.025±0.003	1.8±0.2

Fe-10Cr	Ar	10.2 ±1.5	99.1 ±0.2	0.0097±0.001	3.4±0.5/7.9±0.6
	N_2	9.9 ±1.8	99.1 ±0.1	0.037±0.002	3.2±0.2/7.1±0.6
Fe-15Cr	Ar	15.3 ±1.9	99.3 ±0.2	0.012±0.001	51.6±3.5
	N_2	15.1 ±2.0	99.2 ±0.1	0.021±0.003	21.5±1.8
Fe-24Cr	Ar	24.4 ±2.5	99.2 ±0.2	0.015±0.002	44.3±4.3
	N_2	23.9 ±1.8	99.1 ±0.1	0.062±0.004	28.4±0.5

The measured relative densities (using optical microscopy) of each sample are listed in Table 1. No evident effect of the atmosphere on the porosity could be seen. The N contents in Fe-*x*Cr(N) were measured and listed in Table 1. Compared to the N contents of Fe and Fe46Cr powders (0.0079 and 0.006 wt.%, respectively), those in all the printed Fe-*x*Cr(N) are markedly higher, implying significant N uptake during PBF-LB/M. The uptake of N content in the samples fabricated in the Ar atmosphere is negligible, as shown in Table 1. This is expected, for the following reasons. (i) Both Fe and Fe-46Cr starting powders were gas atomized under an Ar atmosphere and the N contents in these powders are small (0.0079 and 0.006 wt.%, respectively). (ii) Before PBF-LB/M fabrication, high-purity Ar gas (99.999%) was used to purge the chamber and acts as protecting atmosphere.

A careful analysis on the synchrotron results reveals the presence of a trace amount of a hexagonal close packed (HCP) precipitate in Fe-*x*Cr(N) (*x*=5, 10, and 15 wt.%), which should be Cr_2N, the most widely observed nitride in Cr-containing alloys [20,31]. One example of Fe-10Cr(N) is shown in Figures 3(c) and 3(d). Except for the Cr_2N observed using the synchrotron diffraction, it is possible that other types of precipitates that are small in size or volume fraction (or both) exist within the microstructure. Especially the rapid cooling and chemical inhomogeneities that occur during PBF-LB/M can lead to the formation of precipitates that are unanticipated in conventional methods [31]. There are 8 types of precipitates that can form in the Fe-*x*Cr alloys (Table 2), excluding the phases that are not experimentally established or only stable under high pressure, e.g., FeN [32-34], FeN_2 [35], Fe_7N_3 [36], and FeN_4 [37]. Note that oxides are also included in Table 2, because recent studies have revealed that O uptake is inevitable in the PBF-LB/M process (either from the PBF-LB/M chamber or from the oxide layers of the powder [38-41]. To confirm the O uptake, the O contents of the two powder feedstock and the printed samples were measured and listed in Table 3. Evident O contents were detected in the powder feedstocks (compared to nitrogen, which is lower than 0.01 wt.%), and a slight increase can be seen after the PBF-LB/M process. No significant effect of Cr on the oxygen intake can be observed.

Table 2. Structure and lattice parameters of commonly observed Fe/Cr nitrides and oxides.

Phase	Structure and space group	Lattice parameter
ζ-Fe_2N	Orthorhombic, *Pbcn* [42]	a = 4.4373 Å, b = 5.5413 Å, and c = 4.8429 Å [42]
γ′-Fe_4N	Perovskite, $Pm(\bar{3})m$ [42]	a = 3.79Å [42]
α′-Fe_8N	Body-centered tetragonal, *I4/mmm* [43]	a = 2.85 Å and c = 3.09 Å [43]
α″-$Fe_{16}N_2$	Body-centered tetragonal, *I4/mmm* [44]	a = 5.72 Å and c = 6.31 Å [44]
Cr_2N	Hexagonal close packed, *P6(3)/mmc* [45]	a = 4.18 Å and c = 4.44 Å [45]
CrN	NaCl type, $Fm(\bar{3})m$ [46]	a = 4.14 Å [46]
Fe_2O_3	Corundum structure, $R(\bar{3})c$ [47]	a = 5.03 Å and c = 13.75 Å [47]
Cr_2O_3	Corundum structure, $R(\bar{3})c$ [47]	a = 4.95 Å and c = 13.57 Å [47]

Table 3. The O contents of the Fe, Fe-46Cr powders, and the as-printed Fe-*x*Cr alloys (under nitrogen atmosphere).

Condition	Fe powder	Fe-46Cr powder	Fe	Fe-5Cr	Fe-10Cr	Fe-15Cr	Fe-24Cr
O (wt.%)	0.036	0.052	0.055	0.042	0.069	0.044	0.067

Each of the Fe-*x*Cr sample were subjected to TEM to study the morphology and crystal structure of the precipitates in them. The results are shown in Figure 4. Fine and uniformly distributed precipitates were observed in all the samples. The fractions and sizes of the precipitates were estimated and plotted against the Cr content in Figure 5. The following are the observations, made on the basis of Figures 4 and 5. (i) Increasing the Cr content results in a reduction in precipitate size and an increase in their quantity. (ii) In comparison to samples fabricated under the Ar atmosphere, those fabricated under N_2 exhibit a greater fraction of precipitates, albeit with a finer size. (iii) As only oxides are expected in the Ar samples, the increment of the fraction of precipitates in N samples can be attributed to the formation of nitrides. The highest increase in the precipitate fraction was observed in the Fe-15Cr and Fe-24Cr samples. Note that the estimation of precipitate characteristics, displayed in Figure 5, was made according to the contrast of precipitates under TEM. There would be precipitates that are either low in contrast or small in size and thus were not included.

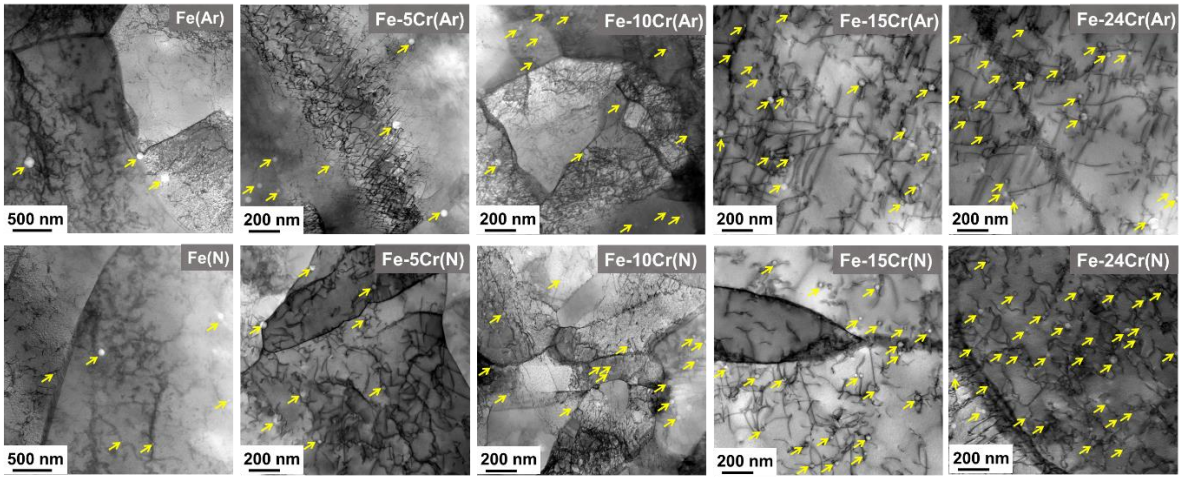

Figure 4. Representative TEM bright field images of Fe-*x*Cr alloys (*x*=0, 5, 10, 15, 24 wt.%), showing disperse precipitates (marked out by yellow arrows).

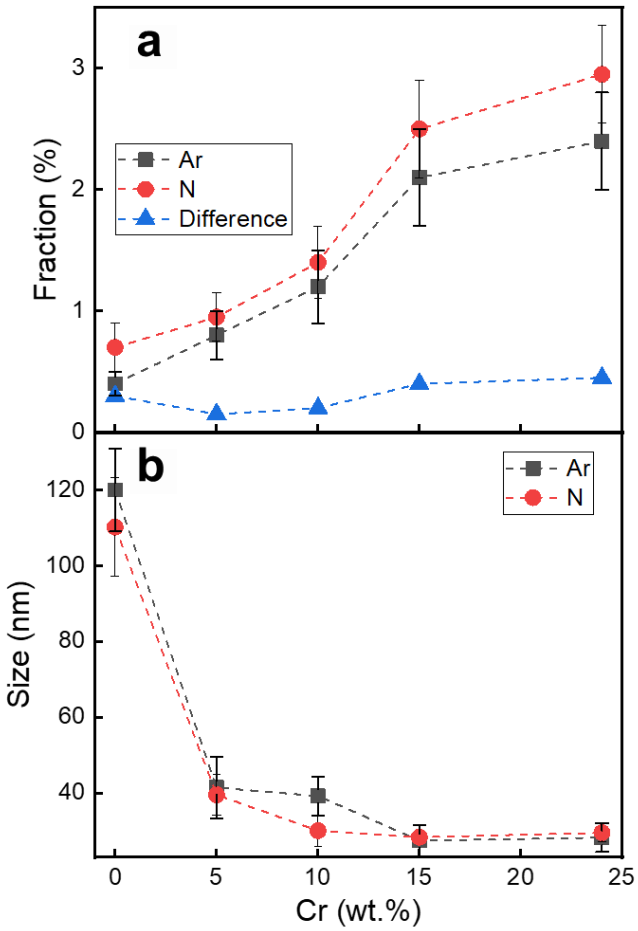

Figure 5. (a) Fractions and (b) average sizes of the precipitates, obtained using TEM, in Fe-*x*Cr alloys (*x*=0, 5, 10, 15, 24 wt.%) fabricated under both N_2 and Ar atmospheres.

TEM-EDS mapping was conducted on each sample to reveal the type of the precipitates, and the representative results, obtained from Fe-24Cr(N), are shown in Figure 6. As seen from

Figure 6(a), which was performed on the precipitates shown in Figure 4, the spherical particles that were commonly observed are confirmed to be oxides (evidenced by the contrast of Oxygen in Figure 6(a_4)). Clear evidence on the existence of nitrides was only found by recourse to EDS mapping at higher magnification, as exemplified by Figure 6(b). It was revealed that Cr nitrides tend to occur predominantly along the grain boundary.

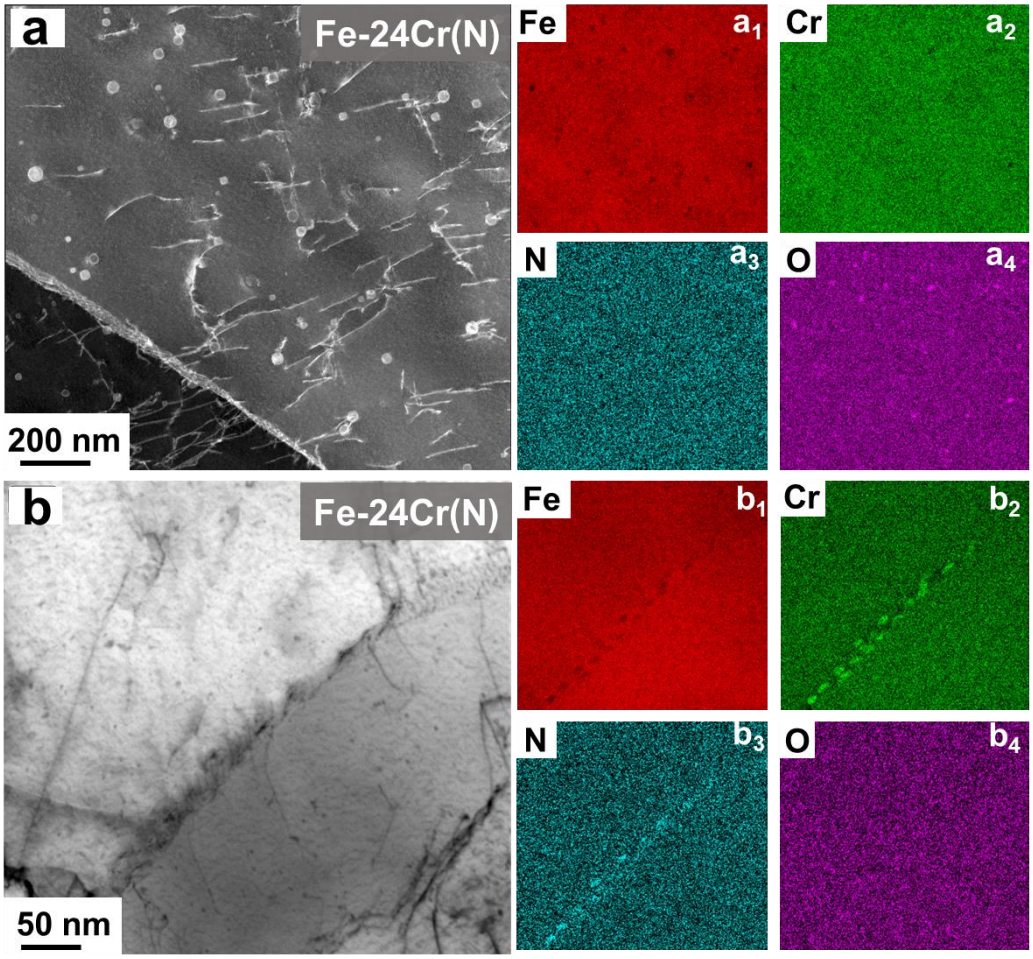

Figure 6. (a) Representative TEM EDS maps on the precipitates, and (b) zoomed-in maps on the nitrides, obtained from Fe-24Cr(N) sample.

Given the complexity of types of precipitates (see Table 2), we did not attempt to identify ALL the precipitates observed in TEM, as it is beyond the scope of the current study. Characterization on one of them, as an example, using high resolution (HR) TEM shows a semi-coherent precipitate/matrix interface, Figure 7(a), with misfit dislocations compensating the inter-planar spacing mismatch. Based on the HRTEM results and corresponding Fast Fourier Transform (FFT) pattern (Figure 7(b)), the precipitate is found to be α′-Fe_8N, exhibiting [001]α//[001]α′ orientation relationship with the matrix.

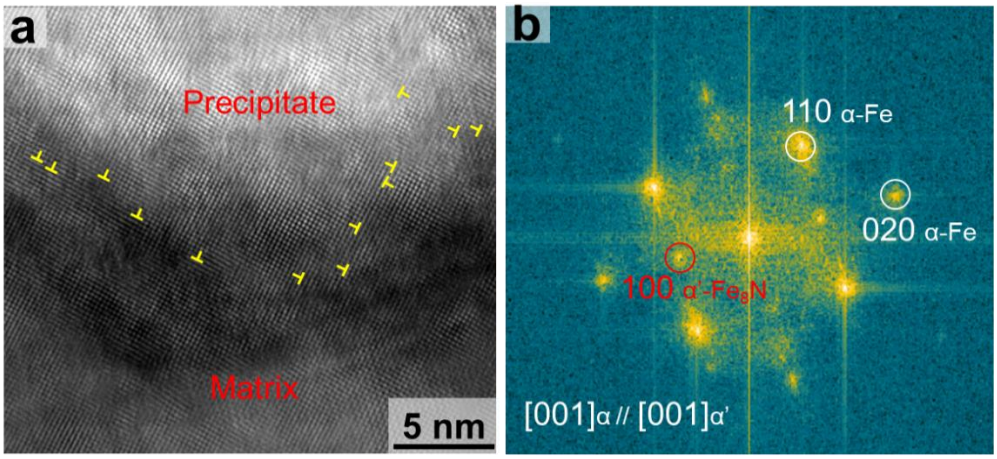

Figure 7. (a) High resolution TEM image of one precipitate and the corresponding FFT pattern.

Understanding nitrogen's solubility in steels and effectively controlling its content, particularly in Cr-containing stainless steels, have long been recognized as crucial for enhancing mechanical properties of steels [20,48]. Typically, nitrogen's solubility in the Fe-Cr alloys is measured using the Sieverts method or the sampling method (gas–liquid metal equilibration technique) [48], where constant temperature and pressure, and sufficient diffusion time are required. Based on such measurements, equations on the nitrogen's solubility: $[N] = a_0 + a_1 * [Cr] + a_2 * P^{\frac{1}{2}} + a_3 * [Cr]^2 + a_4 * [Cr] * P^{\frac{1}{2}}$ (where a_0, a_1, a_2, a_3 and a_4 are interaction coefficients and P is the melt pressure) and the activity coefficient of chromium on nitrogen: $logf_N^{Cr} = e_N^{Cr} * [Cr] + r_N^{Cr} * [Cr]^2$ (where e_N^{Cr} and r_N^{Cr} are the first and the second order interaction parameters of Cr and nitrogen in liquid Fe–Cr alloys), were developed [20,48]. However, during the scanning of the high-power laser with a Gaussian profile, the temperature of the melt varies rapidly and inhomogeneously. Regarding the pressure, due to the interaction of nitrogen atmosphere with the laser and the melt, there would be turbulence in the nitrogen flow and thus unstable pressure. These factors make any estimates of the solubility of N in PBF-LB/M Fe-Cr alloys, using the equations established for conventional alloys, imprecise.

It is known that Cr can substantially increase the N concentration in the steels [20,21]. In a study on the Fe-Cr alloys that are melted in a furnace attached to a hot isostatic press (HIP) furnace that uses nitrogen as the pressurizing gas, it was found that, at atmospheric pressure, N acted as a solute (without forming any nitride) in alloys with 2–20 wt.% Cr [20]. In these alloys, N content increased from 0.05 to 0.22 wt.% [20]. Evidently, these results are in distinct contrast to our findings, as nitrides formed in the as-printed PBF-LB/M samples. Despite the significant effort in characterizing the types and morphologies of the precipitates using Synchrotron and

TEM, there would still be precipitates that are either low in contrast or small in size and thus cannot be well-characterized. Moreover, the complexity in the thermal history of PBF-LB/M would lead to formation of precipitates/phases that are metastable/unstable under conventional fabrication method, thus making it challenging to discuss the stability and formation mechanisms. As the exact amount of N in the nitrides cannot be obtained due to the complexity of nitride type and uncertainty of quantity, the solubility of N in the PBF-LB/M samples cannot be estimated, despite the measured N content in the bulk samples (Table 1). Such difference between the PBF-LB/M and HIP samples can be attributed to the unique way that N_2 gas interacts with the high-energy laser during the PBF-LB/M process. The interaction between laser and N_2 gas is a complex subject, which involves the specifications of laser (i.e., power, wavelength, beam shape, and spot size) and various reactions of N_2 gas (e.g., absorption, scattering, photodissociation, and photoionization). This aspect is beyond the scope of the current study, which will be pursued in the future.

The complexity of melt pool dynamics also makes it challenging to further investigate the effect of Cr content on the interaction between N_2 gas and melt pool. With varying amount of Fe-46Cr powders for each fabrication process, the melt pool shape, surface tension, and the flow characteristics of the liquid are likely to vary significantly [49], resulting in the distinct interactions with the N_2 atmosphere and thus the N content in the Cr containing alloys examined. Moreover, the inevitable chemical heterogeneity that arise during in situ alloying will further complicate this issue. Another aspect that can affect the solidification process and the N uptake is the enthalpy of mixing, which increases with an increasing Cr content [50]. Hence, during the solidification and formation of solid solution in the Fe-*x*Cr alloys, endothermic dissolution reaction occurs to varying degrees, which leads to different temperatures in the molten pool and thus the variations of interaction with N_2 atmosphere. Due to the complexity of the interactions between N atmosphere and the melt pool, the Cr content is no longer the key factor in affecting the N solubility and uptake, which is the reason for the unclear relationship between the overall N and Cr listed in Table 1.

3.2.Microstructure

3.2.1 Variations of grain size/morphologies with Cr content

The crystallographic orientation maps on side surfaces of the Fe-*x*Cr alloys (whose normal is perpendicular to the build direction, BD) characterized using EBSD are shown in Figure 8. The following are the three major aspects that need to be discussed regarding the

microstructures: (i) variations of grain size/morphologies with Cr content, (ii) bimodal grain morphology in the Fe-10Cr sample, and (iii) the effect of printing atmosphere on the grain refinement. Aspect (i) is addressed here, while the remaining two aspects will be discussed in the subsequent subsections. Both Fe and Fe-5Cr fabricated under both Ar and N_2 atmospheres show fine equiaxed grains, while Fe-10Cr exhibit both equiaxed and columnar grains. Further increase of Cr content to 15 and 24 wt.% leads to the formation of columnar grains. The grain sizes, obtained from the EBSD maps, are listed in Table 1.

In AM processes, columnar grains are typically favoured due to the relatively lower energy barrier for epitaxial growth, which implies that the grains in a molten pool nucleate from the previously deposited layer, hence following the same crystallographic orientation as the previous grains (as exemplified by Fe-15Cr(Ar) in Figure 8) [2]. However, there are several approaches that can be utilized to break the occurrence of columnar grains, e.g., altering the thermal history through manipulating fabrication conditions [2], constitutional undercooling [28], additional inoculations as grain nucleation sites [51], and phase transformation [52].

Here, according to the phase diagram, it appears that the α→γ→ α phase transformation plays a key role in the formation of fine equiaxed grains in the Fe, Fe-5Cr, and Fe-10Cr samples, as they are in distinct contrast to the columnar grains in Fe-15Cr and Fe-24Cr ones, where the phase transformation is not expected. Another reason for highlighting the effect of phase transformation is that, among the samples fabricated under the same atmosphere, other grain refinement mechanisms (mentioned above) are largely absent. Of particular note is that, in the range of 0–24 wt.% Cr (see phase diagram in Figure 3(a)), the melting temperature remains constant (slope of the liquidus close to 0) and there is no evident gap between the solidus and liquidus, indicating insignificant chemical partitioning and, thus, negligible constitutional undercooling [28,53].

The α→γ→α phase transformation induced grain refinement is a well-reported phenomenon in conventionally manufactured steels [54-56]. In the case of AM process, the rapid cooling and cycling heating can lead to more complex phenomenon, and the underlying mechanism can be understood through the following aspects. (i) Upon solidification, columnar α grains are favoured due to the rapid cooling and lack of constitutional undercooling. (ii) As the solidified materials cool down, solid-state phase transformations α→γ→ α occur, each of which are accompanied by phase nucleation and change of lattice parameters/volume [52]. The volume change can lead to increase of internal strain, which can be reduced either by elastic-plastic deformation [57] or autocatalytic nucleation of α phase on the migrating γ/α interface [58]. With driving force for grain nucleation and limited time (due to the rapid cooling) for

grain growth, columnar grains are broken down into fine, equiaxed ones [52]. (iii) During the layer-by-layer fabrication process, the high-energy laser can repetitively heat the solidified layers, resulting in iterations of α↔γ phase transformation and further grain refinement.

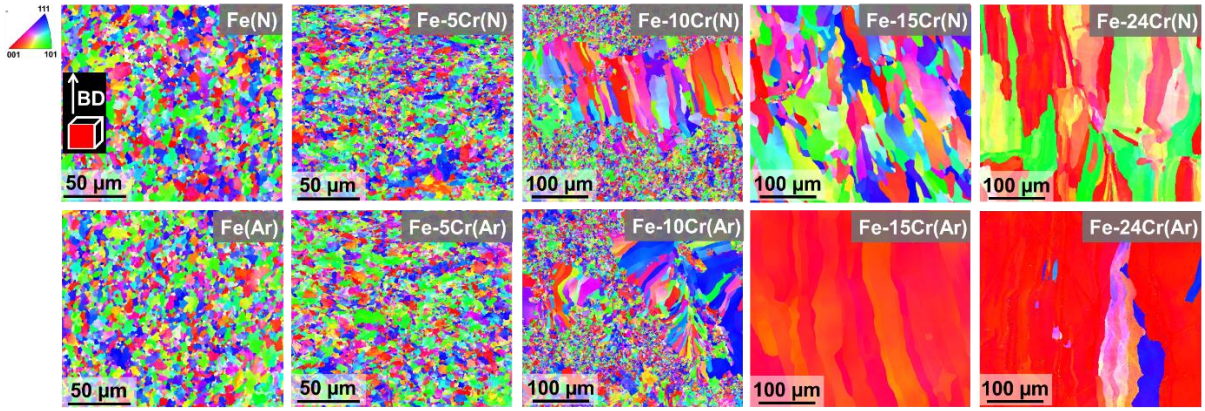

Figure 8. Crystallographic orientation maps of Fe-*x*Cr alloys (*x*=0, 5, 10, 15, 24 wt.%). Frist row shows the samples fabricated under N_2 atmosphere, while second row shows that under Ar.

3.2.2 Chemical heterogeneity and bimodal grain morphology in Fe-10Cr sample

The bimodal grain morphology observed in the Fe-10Cr sample can be rationalized by resource to the chemical heterogeneity that inevitably occurs during in situ alloying (using mixed powders). The formation mechanisms of the chemical heterogeneities can be summarized as follows. (i) When the powder feedstocks have distinct melting points, the one with higher melt point could be retained as un-melted particles and thus lead to severe chemical heterogeneity [24]. (ii) Insufficient physical mixing results in pre-existing clusters of powders and thus chemical segregations [26]. (iii) In cases where the powders are physically well-mixed, distinct physical properties or limited solubility can lead to chemical heterogeneity within the melt pools [27]. (iv) Even when the above mechanisms are not notable, melt pools can capture varying numbers of minor alloy powders and thus lead to inhomogeneous compositions at the local scale [25].

In the present's works context, as two feedstocks, i.e., Fe and Fe-46Cr, have good solubility and similar melting points and are physically well-mixed, the chemical heterogeneity is induced by the mechanism (iv)—varying minor powders in each melt pool. As 10 wt.% is close to the critical value of Cr in determining the occurrence of γ→α phase transformation and thus grain morphology, chemical fluctuations induced during in situ alloying process can lead to distinct grain morphologies. A backscattered electron (BSE) image of the Fe-10Cr(N) and the corresponding EDS line scans are shown in Figure 9. It is observed that coarse grains

correspond to higher Cr content, while fine grains are of lower Cr content. Note that the chemical heterogeneity discussed here is inherent to the in situ alloying process (using mixed powders) where the melt pools can capture various numbers of minor particles. Therefore, it is expected in all the samples. Fe-10Cr is a critical composition where the effect of chemical heterogeneity can be highlighted through γ→α phase transformation and, thus, grain morphologies. It is also worth noting that the chemical heterogeneity can also exert influence on the local solubility of N, formation of nitrides, etc. These aspects will be further investigated in future.

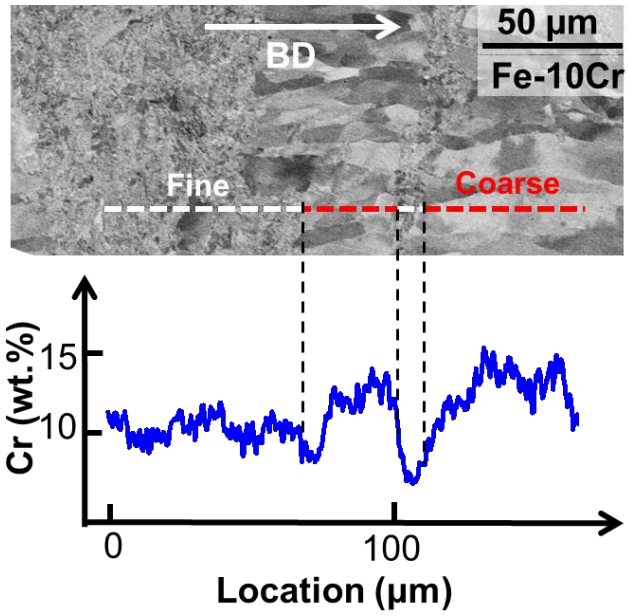

Figure 9. Backscattered electron image on Fe-10Cr sample fabricated under nitrogen atmosphere and the corresponding EDS line scan covering both coarse and fine grains.

3.2.3 Effect of printing atmosphere on the microstructures

As shown in Figure 10, the relative grain refinement in the Fe, Fe-5Cr, and Fe-10Cr samples that were processed under N_2 atmosphere (compared to those processed under Ar) is insignificant. This is because equiaxed grains were observed in these alloys, irrespective of the atmosphere used. The relative grain refinement is more pronounced in the Fe-15Cr and Fe-24Cr samples with columnar grains when processed in Ar. There are two probable grain refinement mechanisms. (i) The precipitates, i.e., nitrides, that formed in situ during the solidification process (including remelting and re-solidification) can act as grain nucleation sites and thus suppress the epitaxial growth and formation of columnar grains [59]. (ii) The differences in the thermophysical properties, e.g., specific heat, gas constant, and thermal

conductivity, of the two atmospheres results in the variations of the thermal history during the solidification and thus varying microstructures. Recent studies have revealed that the N_2 and Ar atmospheres can lead to different thermodynamics and kinetics of the melt pool and the evaporation flow, resulting in varying porosity and microstructures [13,60], which supports the above argument.

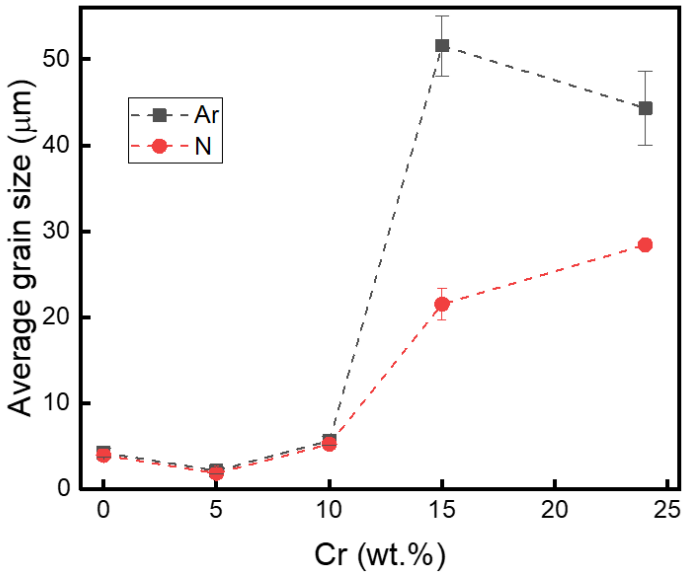

Figure 10. Grain sizes, obtained using EBSD, of Fe-*x*Cr alloys (*x*=0, 5, 10, 15, 24 wt.%) fabricated under both N_2 and Ar atmospheres.

3.3. Cracking

Micro-cracks were found in Fe-15Cr(N) and Fe-24Cr(N) samples in the as-printed state. Typical morphologies of the cracks are shown in Figure 11, where cracks both parallel and perpendicular to BD were observed. The straightness of the cracks indicates they propagated without interacting with the microstructure. Since solidification and liquation cracks typically occur along grain/dendrite boundaries [61,62] and heat-affected zones, respectively [63], the observed crack morphology suggests that they are residual stress induced cracks. As cracking was not observed in Fe-15Cr(Ar) and Fe-24Cr(Ar), N_2 atmosphere must be one of the key factors in inducing the cracking in Fe-15Cr(N) and Fe-24Cr(N), either via causing brittleness or exacerbating residual stress. With an increase in the Cr content, an overall increase in the precipitate content can be expected, given the low enthalpy of forming Cr-N bond (-117 kJ/mol[64]). A higher fraction of precipitates (than in Fe-10Cr(N)) in Fe-15Cr(N) and Fe-24Cr(N), as evidenced by Figures 4 and 5, can lead to hardening and embrittlement, eventually resulting in cracking in the presence of the residual stress that arise during and/or after

solidification. The microstructures of Fe-15Cr and Fe-24Cr could be another factor for the formation of cracking. More specifically, the columnar grains in Fe-15Cr and Fe-24Cr make them less resistant to crack growth, compared to the samples with finer grains [65]. γ→α phase transformation plays a significant role in affecting the residual stress, as it is closely associated with volume change and dislocation mobility [66,67]. Hence, the absence of this phase transformation in the Fe-15Cr and Fe-24Cr alloys may contribute to elevated levels of residual stress in these alloys, compared to the others. When combined with the presence of columnar grains and precipitates, these factors could be significant contributors to the observed cracking in these two samples.

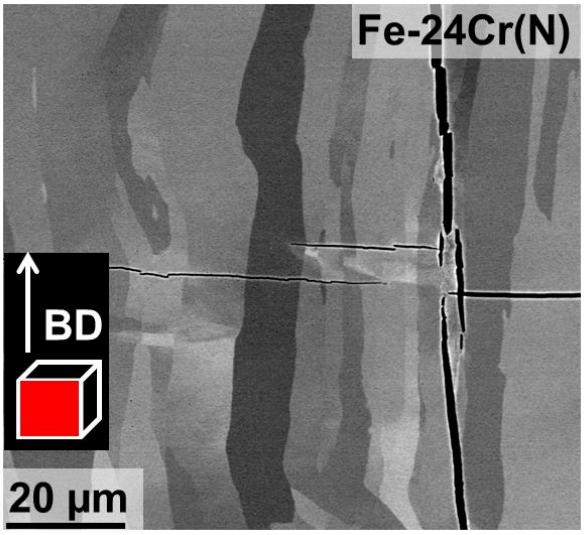

Figure 11. Cracks observed in Fe-24Cr(N) sample, both parallel and perpendicular to the BD.

3.4. Mechanical properties

Representative engineering stress-strain responses of the printed alloys, tensile tested in the parallel and vertical orientations (with respect to BD) are shown in Figures 12(a) and 12(b), respectively. The average ultimate tensile strength (σ_{UTS}) and yield strength (σ_y) extracted from the results are plotted against the Cr content in Figures 12(c) and 12(d), respectively. (As already mentioned, both Fe-15Cr(N) and Fe-24Cr(N) are cracked in the as-printed state and thus meaningful tensile tests could not be conducted. No crack was observed in other samples.) The following are some key observations. (i) The anisotropy in strength in any sample is insignificant (less than 5%). Therefore, the properties of vertical and parallel orientations will not be distinguished hereafter. (ii) Compared to their Ar counterparts, significant enhancements of both σ_y and σ_{UTS} are seen in Fe(N), Fe-5Cr(N), and Fe-10Cr(N), which could be due to the collective effects of solid solution strengthening caused by N and

the precipitation strengthening by nitrides. (iii) Among the samples fabricated under Ar atmosphere, Fe-5Cr(Ar) shows the highest σ_y and σ_{UTS}, due to grain boundary strengthening associated with the fine equiaxed grains (Figure 10). When N_2 atmosphere was utilized, highest σ_{UTS} is seen in Fe-10Cr(N) sample, while maximum σ_y is obtained in Fe-5Cr(N) sample. (iv) Except for inducing hot cracking and, thus premature failure in Fe-15Cr(N) and Fe-24Cr(N) samples, the effect of N_2 atmosphere on the uniform elongation (until σ_{UTS}) is insignificant. In some of the conditions, e.g., the Fe-5Cr and Fe-10Cr parallel, samples fabricated under N_2 atmosphere show lower elongation to failure than those under Ar, but similar uniform elongation. (v) Yield point phenomenon was observed in the Fe and Fe-5Cr samples, under both printing atmospheres. This phenomenon in steels is well-known and can be attributed to the Cottrell atmosphere induced by interstitial atoms (i.e., carbon, oxygen, and nitrogen) [68]. TEM-EDS maps have shown the dissolved N and O atoms in Figure 6, which could contribute to the formation of the Cottrell atmospheres around dislocation cores. However, TEM-EDS mapping only offers qualitative results on light elements, making the exact amount of dissolved N unavailable. Upon deformation, interstitial atoms can segregate to dislocations, form the Cottrell atmospheres, which, in turn, pin the dislocations, leading to a higher energy barrier for dislocation motion [68]. Once the dislocations are unpinned from the Cottrell atmosphere through the application of a higher stress, they multiply rapidly, which results in lowered flow stress. Compared to low-alloy steels, yield point phenomenon is less evident in the steels with high contents of the alloying elements e.g., Fe-10Cr, Fe-15Cr, and Fe-24Cr alloys, due to the dominance of the alloying elements on the microstructure and mechanical properties of the materials, e.g., solid solution strengthening and precipitation hardening. Therefore, the onset of plastic deformation could be more gradual instead of a distinct yield point. As shown in Figure 12, the yield point phenomenon is less evident in Fe-5Cr than Fe and cannot be seen in the samples with Cr content $\geqslant$ 10 wt.%. Except for the nitrogen from the printing atmosphere, oxygen (either from the PBF-LB/M chamber or the oxide layer of the powders) can dissolve into the alloy and cause a yield plateau.

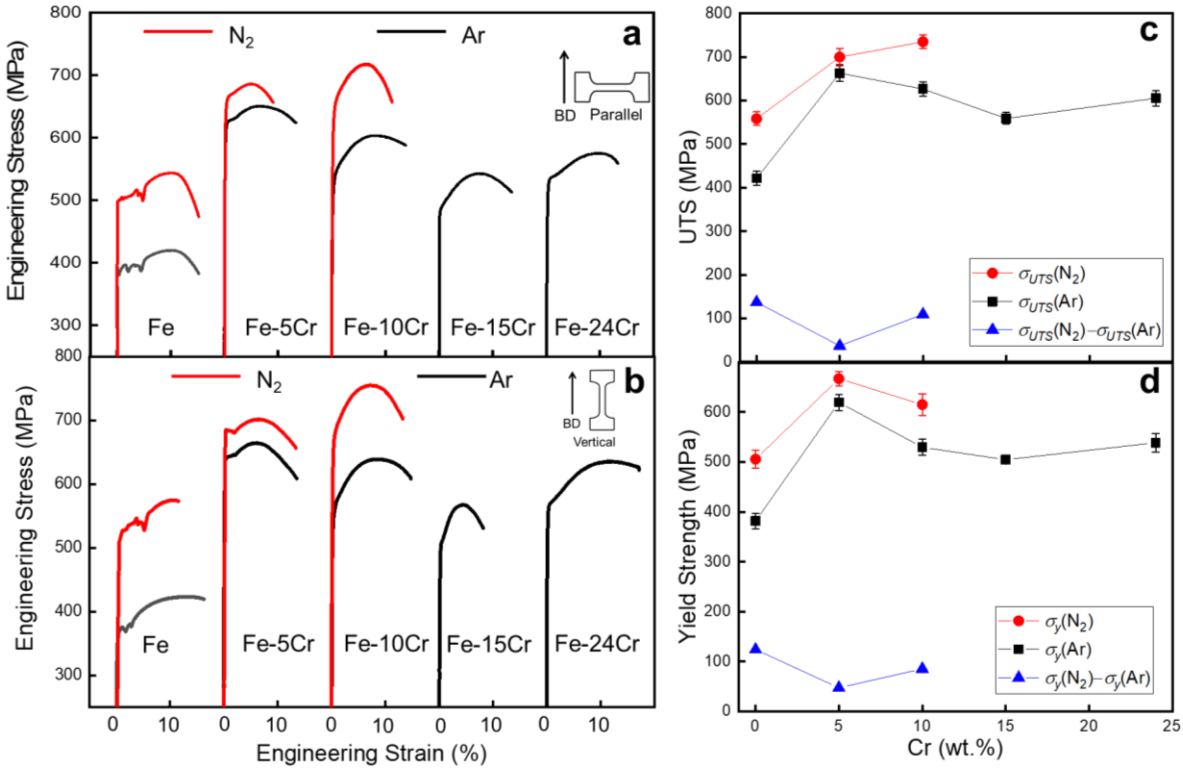

Figure 12. Representative engineering stress-strain curves of Fe-*x*Cr alloys (*x*=0, 5, 10, 15, 24 wt.%), fabricated under both N_2 and Ar atmospheres. Tensile testing was conducted along two orientations (a) parallel and (b) vertical, as schematically shown in the figure. Plots of σ_{UTS} (c) and σ_y (d) against Cr content. The difference between samples under N_2 and Ar atmospheres are also given.

4. Summary

In summary, Fe-*x*Cr (*x*=0, 5, 10, 15, 24 wt.%) alloys were fabricated under both Ar and N_2 atmospheres to study the effect of nitrogen uptake during PBF-LB/M on the microstructures and mechanical properties. PBF-LB/M performed under the N_2 atmosphere leads to the formation of Cr and Fe nitrides in the alloy. Both Fe and Fe-5Cr possess fine and equiaxed grains, irrespective of the atmosphere used, due to the γ→α phase transformation during cooling. Bimodal grain morphologies are seen in Fe-10Cr, induced by the melt-pool-scale chemical heterogeneity. Strongly textured columnar grains are seen in Fe-15Cr(Ar) and Fe-24Cr(Ar), while N_2 atmosphere significantly refines the grain size and weakens the texture. Evident enhancement of strength was observed in Fe(N), Fe-5Cr(N), and Fe-10Cr(N) due possibly to solid solution and precipitation strengthening caused by N. The combination of columnar grain morphology, larger precipitate volume fraction, and residual stress lead to embrittlement of Fe-15Cr(N) and Fe-24Cr(N). Results of this study demonstrate that the

nitrogen atmosphere exerts a significant influence on the microstructure and mechanical properties of Fe-Cr alloys, insights of which can be applied to other classes of alloys.

Acknowledgement

This work was supported by Agency for Science, Technology and Research (A*STAR) of Singapore via the Structural Metal Alloys Programme (No. A18B1b0061) and the Individual Research Grant (Grant reference No.: A20E7c0109). We would like to acknowledge the contribution of Ms. Jing Jun Lee on the EBSD characterization, Mr Jethro Tong on samples preparation, and Dr Fatih Uzun on the synchrotron testing. Authors also appreciate the beam time allocated to them under award MG31917-1 at the Diamond Light Source (UK).

References

[1] S. Wei, C. Hutchinson, U. Ramamurty, Mesostructure engineering in additive manufacturing of alloys, Scripta Materialia 230 (2023) 115429.
[2] T. DebRoy, H. L. Wei, J. S. Zuback, T. Mukherjee, J. W. Elmer, J. O. Milewski, A. M. Beese, A. Wilson-Heid, A. De, W. Zhang, Additive manufacturing of metallic components – Process, structure and properties, Progress in materials science 92 (2018) 112-224.
[3] S.-H. Li, P. Kumar, S. Chandra, U. Ramamurty, Directed energy deposition of metals: processing, microstructures, and mechanical properties, International Materials Reviews (2022) 1-43.
[4] A. Chniouel, P.-F. Giroux, F. Lomello, P. Aubry, É. Vasquez, O. Hercher, H. Maskrot, Influence of substrate temperature on microstructural and mechanical properties of 316L stainless steel consolidated by laser powder bed fusion, The International Journal of Advanced Manufacturing Technology 111 (2020) 3489-3503.
[5] Z. Tian, C. Zhang, D. Wang, W. Liu, X. Fang, D. Wellmann, Y. Zhao, Y. Tian, A review on laser powder bed fusion of inconel 625 nickel-based alloy, Applied Sciences 10 (2019) 81.
[6] H. Zhou, C. Song, Y. Yang, C. Han, M. Wang, Y. Xiao, Z. Liu, The microstructure and properties evolution of SS316L fabricated by magnetic field-assisted laser powder bed fusion, Materials Science and Engineering: A 845 (2022) 143216.
[7] C. J. Todaro, M. A. Easton, D. Qiu, D. Zhang, M. J. Bermingham, E. W. Lui, M. Brandt, D. H. StJohn, M. Qian, Grain structure control during metal 3D printing by high-intensity ultrasound, Nat Commun 11 (2020) 142.
[8] L. Liu, C. Chen, R. Zhao, X. Wang, H. Tao, S. Shuai, J. Wang, H. Liao, Z. Ren, In-situ nitrogen strengthening of selective laser melted Ti6Al4V with superior mechanical performance, Additive Manufacturing 46 (2021).
[9] Y. Xiao, Y. Yang, D. Wang, L. Liu, Z. Liu, S. Wu, H. Zhou, Z. Liu, C. Song, In-situ synthesis of high strength and toughness TiN/Ti6Al4V sandwich composites by laser powder bed fusion under a nitrogen-containing atmosphere, Composites Part B: Engineering 253 (2023).
[10] H. Amano, T. Ishimoto, R. Suganuma, K. Aiba, S.-H. Sun, R. Ozasa, T. Nakano, Effect of a helium gas atmosphere on the mechanical properties of Ti-6Al-4V alloy built with laser powder bed fusion: A comparative study with argon gas, Additive Manufacturing 48 (2021) 102444.
[11] Y. Yang, J. Zhang, W. Wei, Microstructure and mechanical properties of TiC/Ti6Al4V nanocomposites fabricated by gas–liquid reaction laser powder bed fusion, Materials Science and Engineering: A 869 (2023) 144829.
[12] V. G. Gavriljuk, H. Berns. *High nitrogen steels: structure, properties, manufacture, applications*. (Springer Science & Business Media, 1999).
[13] J. Boes, A. Röttger, W. Theisen, Microstructure and properties of high-strength C + N austenitic stainless steel processed by laser powder bed fusion, Additive Manufacturing 32 (2020).
[14] B. D. Shanina, V. G. Gavriljuk, H. Berns, F. Schmalt, Concept of a new high‐strength austenitic stainless steel, Steel research 73 (2002) 105-113.
[15] W. Tong, N. Tao, Z. Wang, J. Lu, K. Lu, Nitriding iron at lower temperatures, Science 299 (2003) 686-688.
[16] P. Schaaf, Laser nitriding of metals, Progress in materials science 47 (2002) 1-161.
[17] B. Cheng, F. Wei, W. H. Teh, J. J. Lee, T. L. Meng, K. B. Lau, L. T. Chew, Z. Zhang, K. H. Cheong, C. K. Ng, P. Wang, C. C. Tan, U. Ramamurty, Ambient pressure fabrication of Ni-

free high nitrogen austenitic stainless steel using laser powder bed fusion method, Additive Manufacturing 55 (2022).
[18] J. Boes, A. Röttger, W. Theisen, C. Cui, V. Uhlenwinkel, A. Schulz, H. W. Zoch, F. Stern, J. Tenkamp, F. Walther, Gas atomization and laser additive manufacturing of nitrogen-alloyed martensitic stainless steel, Additive Manufacturing 34 (2020).
[19] C. Cui, V. Uhlenwinkel, A. Schulz, H.-W. Zoch, Austenitic Stainless Steel Powders with Increased Nitrogen Content for Laser Additive Manufacturing, Metals 10 (2020) 61.
[20] J. C. Rawers, N. A. Gokcen, R. D. Pehlke, High nitrogen concentration in Fe-Cr-Ni alloys, Metallurgical Transactions A 24 (1993) 73-82.
[21] M. A. J. Somers, R. M. Lankreijer, E. J. Mittemeijer, Excess nitrogen in the ferrite matrix of nitrided binary iron-based alloys, Philosophical Magazine A 59 (1989) 353-378.
[22] R. Schacherl, P. Graat, E. Mittemeijer, The nitriding kinetics of iron-chromium alloys; the role of excess nitrogen: Experiments and modelling, Metallurgical and materials transactions A 35 (2004) 3387-3398.
[23] B. H. Toby, R. B. Von Dreele, GSAS-II: the genesis of a modern open-source all purpose crystallography software package, Journal of Applied Crystallography 46 (2013) 544-549.
[24] S. Huang, R. L. Narayan, J. H. K. Tan, S. L. Sing, W. Y. Yeong, Resolving the porosity-unmelted inclusion dilemma during in-situ alloying of Ti34Nb via laser powder bed fusion, Acta Materialia 204 (2021) 116522.
[25] H. Li, S. Thomas, C. Hutchinson, Delivering microstructural complexity to additively manufactured metals through controlled mesoscale chemical heterogeneity, Acta Materialia 226 (2022) 117637.
[26] S. Wei, Y. Zhao, B. Zhang, P. Wang, U. Ramamurty, Mesoscopic chemical heterogeneities in laser powder bed fused CoCrMo and Ni mixed powders and their effect on the mechanical properties, Materials Science and Engineering: A 888 (2023) 145795.
[27] T. Zhang, Z. Huang, T. Yang, H. Kong, J. Luan, A. Wang, D. Wang, W. Kuo, Y. Wang, C.-T. Liu, In situ design of advanced titanium alloy with concentration modulations by additive manufacturing, Science 374 (2021) 478-482.
[28] S. Wei, K. B. Lau, J. J. Lee, F. Wei, W. H. Teh, B. Zhang, C. C. Tan, P. Wang, U. Ramamurty, Selective laser melting of Fe–Al alloys with simultaneous gradients in composition and microstructure, Materials Science and Engineering: A 821 (2021) 141608.
[29] D. Zhang, D. Qiu, M. A. Gibson, Y. Zheng, H. L. Fraser, D. H. StJohn, M. A. Easton, Additive manufacturing of ultrafine-grained high-strength titanium alloys, Nature 576 (2019) 91-95.
[30] H. Okamoto, T. Massalski, Binary alloy phase diagrams, ASM International, Materials Park, OH, USA 12 (1990).
[31] N. Haghdadi, H. Chen, Z. Chen, S. S. Babu, X. Liao, S. P. Ringer, S. Primig, Intergranular precipitation and chemical fluctuations in an additively manufactured 2205 duplex stainless steel, Scripta Materialia 219 (2022) 114894.
[32] K. Suzuki, H. Morita, T. Kaneko, H. Yoshida, H. Fujimori, Crystal structure and magnetic properties of the compound FeN, Journal of Alloys and Compounds 201 (1993) 11-16.
[33] H. Nakagawa, S. Nasu, H. Fujii, M. Takahashi, F. Kanamaru, 57 Fe Mössbauer study of FeN x (x= 0.25≈ 0.91) alloys, Hyperfine Interactions 69 (1992) 455-458.
[34] W. P. Clark, S. Steinberg, R. Dronskowski, C. McCammon, I. Kupenko, M. Bykov, L. Dubrovinsky, L. G. Akselrud, U. Schwarz, R. Niewa, High-Pressure NiAs-Type Modification of FeN, Angewandte Chemie International Edition 56 (2017) 7302-7306.
[35] D. Laniel, A. Dewaele, G. Garbarino, High pressure and high temperature synthesis of the iron pernitride FeN2, Inorganic chemistry 57 (2018) 6245-6251.
[36] S. Minobe, Y. Nakajima, K. Hirose, Y. Ohishi, Stability and compressibility of a new iron-nitride β-Fe7N3 to core pressures, Geophysical Research Letters 42 (2015) 5206-5211.

[37] M. Bykov, E. Bykova, G. Aprilis, K. Glazyrin, E. Koemets, I. Chuvashova, I. Kupenko, C. McCammon, M. Mezouar, V. Prakapenka, Fe-N system at high pressure reveals a compound featuring polymeric nitrogen chains, Nature communications 9 (2018) 2756.
[38] S. Wei, P. Kumar, K. B. Lau, D. Wuu, L.-L. Liew, F. Wei, S. L. Teo, A. Cheong, C. K. Ng, B. Zhang, C. C. Tan, P. Wang, U. Ramamurty, Effect of heat treatment on the microstructure and mechanical properties of 2.4 GPa grade maraging steel fabricated by laser powder bed fusion, Additive Manufacturing 59 (2022) 103190.
[39] X. Lou, P. L. Andresen, R. B. Rebak, Oxide inclusions in laser additive manufactured stainless steel and their effects on impact toughness and stress corrosion cracking behavior, Journal of Nuclear Materials 499 (2018) 182-190.
[40] W. A. Grell, E. Solis-Ramos, E. Clark, E. Lucon, E. J. Garboczi, P. K. Predecki, Z. Loftus, M. Kumosa, Effect of powder oxidation on the impact toughness of electron beam melting Ti-6Al-4V, Additive Manufacturing 17 (2017) 123-134.
[41] S. Wei, Y. Zhao, S.-H. Li, S. Chen, K. B. Lau, V. Soh, J. J. Lee, B. Zhang, C. C. Tan, P. Wang, U. Ramamurty, Laser powder bed fusion of a Cu-Ni-Al alloy using the compositional grading approach, Scripta Materialia 231 (2023) 115441.
[42] K. H. Jack, Binary and ternary interstitial alloys I. The iron-nitrogen system: The structures of Fe4N and Fe2N, Proceedings of the Royal Society of London. Series A. Mathematical and Physical Sciences 195 (1948) 34-40.
[43] K. H. Jack, The iron-nitrogen system: the preparation and the crystal structures of nitrogen-austenite (γ) and nitrogen-martensite (α'), Proceedings of the Royal Society of London. Series A. Mathematical and Physical Sciences 208 (1951) 200-215.
[44] K. H. Jack, The occurrence and the crystal structure of α"-iron nitride; a new type of interstitial alloy formed during the tempering of nitrogen-martensite, Proceedings of the Royal Society of London. Series A. Mathematical and Physical Sciences 208 (1951) 216-224.
[45] F. Vanderschaeve, R. Taillard, J. Foct, Discontinuous precipitation of Cr2N in a high nitrogen, chromium-manganese austenitic stainless steel, Journal of Materials Science 30 (1995) 6035-6046.
[46] F. Rivadulla, M. Bañobre-López, C. X. Quintela, A. Piñeiro, V. Pardo, D. Baldomir, M. A. López-Quintela, J. Rivas, C. A. Ramos, H. Salva, Reduction of the bulk modulus at high pressure in CrN, Nature Materials 8 (2009) 947-951.
[47] E. Verwey, The crystal structure of γ-Fe2O3 and γ-Al2O3, Zeitschrift für Kristallographie-Crystalline Materials 91 (1935) 65-69.
[48] W.-Y. Kim, C.-O. Lee, C.-W. Yun, J.-J. Pak, Effect of chromium on nitrogen solubility in liquid Fe–Cr alloys containing 30 mass% Cr, ISIJ international 49 (2009) 1668-1672.
[49] L. Yao, S. Huang, U. Ramamurty, Z. Xiao, On the formation of “Fish-scale” morphology with curved grain interfacial microstructures during selective laser melting of dissimilar alloys, Acta Materialia 220 (2021) 117331.
[50] M. Levesque, E. Martínez, C.-C. Fu, M. Nastar, F. Soisson, Simple concentration-dependent pair interaction model for large-scale simulations of Fe-Cr alloys, Physical Review B 84 (2011).
[51] J. H. Martin, B. D. Yahata, J. M. Hundley, J. A. Mayer, T. A. Schaedler, T. M. Pollock, 3D printing of high-strength aluminium alloys, Nature 549 (2017) 365-369.
[52] P. Lejček, M. Roudnická, J. Čapek, D. Dvorský, J. Drahokoupil, D. Šimek, J. Čížek, P. Svora, O. Molnárová, D. Vojtěch, Selective laser melting of pure iron: Multiscale characterization of hierarchical microstructure, Materials Characterization 154 (2019) 222-232.
[53] W. A. Tiller, K. A. Jackson, J. W. Rutter, B. Chalmers, The redistribution of solute atoms during the solidification of metals, Acta Metallurgica 1 (1953) 428-437.
[54] M. Gouné, F. Danoix, J. Ågren, Y. Bréchet, C. R. Hutchinson, M. Militzer, G. Purdy, S. van Der Zwaag, H. Zurob, Overview of the current issues in austenite to ferrite transformation

and the role of migrating interfaces therein for low alloyed steels, Materials Science and Engineering: R: Reports 92 (2015) 1-38.
[55] R. W. K. Honeycombe, R. F. Mehl, Transformation from austenite in alloy steels, Metallurgical Transactions A 7 (1976) 915-936.
[56] R. Bengochea, B. Lopez, I. Gutierrez, B. López, I. Gutierrez, Microstructural evolution during the austenite-to-ferrite transformation from deformed austenite, Metallurgical and materials transactions A 29 (1998) 417-426.
[57] S. J. Song, F. Liu, Z. H. Zhang, Analysis of elastic–plastic accommodation due to volume misfit upon solid-state phase transformation, Acta Materialia 64 (2014) 266-281.
[58] Y. Liu, F. Sommer, E. J. Mittemeijer, Abnormal Austenite-Ferrite Transformation Kinetics of Ultra-Low-Nitrogen Fe-N Alloy, Metallurgical and materials transactions A 39 (2008) 2306-2318.
[59] J. H. Martin, B. Yahata, J. Mayer, R. Mone, E. Stonkevitch, J. Miller, R. Mark, T. Schaedler, J. Hundley, P. Callahan, Grain refinement mechanisms in additively manufactured nano-functionalized aluminum, Acta Materialia 200 (2020) 1022-1037.
[60] D. Dai, D. Gu, Effect of metal vaporization behavior on keyhole-mode surface morphology of selective laser melted composites using different protective atmospheres, Applied Surface Science 355 (2015) 310-319.
[61] S. Chandra, X. Tan, R. L. Narayan, C. Wang, S. B. Tor, G. Seet, A generalised hot cracking criterion for nickel-based superalloys additively manufactured by electron beam melting, Additive Manufacturing 37 (2021) 101633.
[62] F. Wei, S. Wei, K. B. Lau, W. H. Teh, J. J. Lee, H. L. Seng, C. C. Tan, P. Wang, U. Ramamurty, Compositionally graded AlxCoCrFeNi high-entropy alloy manufactured by laser powder bed fusion, Materialia 21 (2022) 101308.
[63] H. Ghasemi-Tabasi, C. de Formanoir, S. Van Petegem, J. Jhabvala, S. Hocine, E. Boillat, N. Sohrabi, F. Marone, D. Grolimund, H. Van Swygenhoven, R. E. Logé, Direct observation of crack formation mechanisms with operando Laser Powder Bed Fusion X-ray imaging, Additive Manufacturing 51 (2022) 102619.
[64] F. Tessier, M. R. Ranade, A. Navrotsky, R. Niewa, F. J. DiSalvo, A. Leineweber, H. Jacobs, Thermodynamics of formation of binary and ternary nitrides in the system Ce/Mn/N, Zeitschrift für anorganische und allgemeine Chemie 627 (2001) 194-200.
[65] P. Kumar, O. Prakash, U. Ramamurty, Micro-and meso-structures and their influence on mechanical properties of selectively laser melted Ti-6Al-4V, Acta Materialia 154 (2018) 246-260.
[66] D. Deng, FEM prediction of welding residual stress and distortion in carbon steel considering phase transformation effects, Materials & Design 30 (2009) 359-366.
[67] P. Taraphdar, R. Kumar, C. Pandey, M. Mahapatra, Significance of finite element models and solid-state phase transformation on the evaluation of weld induced residual stresses, Metals and Materials International 27 (2021) 3478-3492.
[68] A. H. Cottrell, B. A. Bilby, Dislocation theory of yielding and strain ageing of iron, Proceedings of the Physical Society. Section A 62 (1949) 49-62 308.